Research Paper

Spatial inhomogeneity of build defects across the build plate in laser powder bed fusion

T.P. Moran [a], D.H. Warner [b,*], A. Soltani-Tehrani [c,d], N. Shamsaei [c,d], N. Phan [e]

[a] Cornell Fracture Group, Sibley School of Mechanical and Aerospace Engineering, Cornell University, Ithaca, NY 14853, United States
[b] Cornell Fracture Group, School of Civil and Environmental Engineering, Cornell University, Ithaca, NY 14853, United States
[c] National Center for Additive Manufacturing Excellence (NCAME), Auburn University, Auburn, AL 36849, United States
[d] Department of Mechanical Engineering, Auburn University, Auburn, AL 36849, United States
[e] Structures Division, Naval Air Systems Command, Patuxent River, MD 20670, United States

ABSTRACT

The population of build defects as a function of position on the build plate was examined in Ti-6Al-4V specimens fabricated on two common commercial laser powder bed fusion (LPBF) systems. Using standard build parameters, X-ray computed tomography revealed that spatial heterogeneity of the defect population can be substantial, relative to the variations in defect population that can occur due to other parameters, e.g. part geometry, build orientation, and laser power schedule. To understand the potential importance of such variability, its impact on fatigue performance is considered. Asymmetries inherent to LPBF fabrication are investigated as potential sources of the spatial heterogeneity, with shielding gas flow simulations providing an explanation.

1. Introduction

Metal additive manufacturing (AM) is a rapidly emerging technology with the potential to displace traditional fabrication methods in several industries [1–4]. Currently, the most common subset of metal AM is laser powder bed fusion (LPBF) [5]. During LPBF, a laser is used to selectively fuse metal particles together, forming a solid component layer-by-layer. LPBF requires an inert build environment of argon or nitrogen-rich gas. This gas is streamed over the build plate to inhibit oxidation and remove by-products at the laser-powder interaction zone. Although this manufacturing technique can provide benefits when compared to traditional manufacturing, an industry aversion to fracture critical implementation exists due to ubiquitous defect populations found in LPBF components [6].

One indicator of the likelihood for defect formation is non-optimal thermal fields surrounding the melt pool. If the input energy is too low, the melt pool will shrink. This can create regions of insufficient melt overlap, which contain unmelted powder particles and inadequate adherence between layers, known as lack of fusion defects [7–9]. Inversely, if the input energy is too high, defects resulting from melt pool instabilities will dominate (e.g. powder displacement, molten ejection due to recoil pressure, and keyhole formation) [10–13,14,15]. These defect populations are detrimental to the mechanical performance and reliability of LPBF components, specifically with regard to fatigue life [16–19,20,21]. For this reason, the ability to predict, and thus reduce, defect populations is critical for the maturation of LPBF technology.

Substantial efforts have been made to correlate defect formation to the prescribed power schedule during LPBF (e.g. laser power, scan speed, and scan strategy). Several studies have attempted to find optimal build parameters by investigating the melt bead characteristics of single-scans across a powder layer with varied laser parameters. These works produce LPBF process maps, with most reliant on the concept of melt pool energy density [22–25,26]. Component scale studies have also been performed to examine the influence of scanning strategy, geometry, build orientation, and heat buildup on defect populations [27–30,31, 32]. These studies are tedious and expensive to perform; thus, conjugate computational models have been pursued to mirror experimentation [33–36]. The scale of these models ranges from fluid dynamics and solidification models of the melt pool to predicting defect distributions due to power schedule and build specific variables at the component scale. These models focus on the effects of prescribed build parameters (e.g. power schedule, build strategy, component geometry, and build orientation) on fabrication quality, without the consideration of the stochastic and systemic aspects of defect formation in LPBF systems.

Although improving build parameters in an effort to decrease defect formation is critical, and thus deserving of such an intensive research

---

effort, we are unaware of published studies focused on the baseline variability of defect formation during a LPBF build. Specifically, a need remains to quantify defect distribution fluctuations expected during fabrication due to variables beyond the prescribed build parameters. To determine the significance of this point, two single sets of titanium specimens from previous projects, fabricated on different commercial LPBF machines, were examined. Computed tomographic (CT) analysis was performed on both sets of specimens to quantify the defect population across the build plate. The importance of the measured spatial variability was quantified by considering high cycle fatigue performance within the context of a weakest link model [19]. Lastly, the variability was examined relative to asymmetrical aspects of LPBF machines (e.g. re-coating, laser incidence angle, and the shielding gas velocity field).

2. Materials and methods

2.1. Specimen fabrication

Two single sets of Ti-6Al-4V specimens were fabricated from two common commercial LPBF machines: the EOS M290 and the 3D Systems ProX DMP320. The M290 build envelope is 250×250×325mm (WxDxH) with a high speed steel blade re-coating system that deposits powder moving right to left; adhering to the frame of reference suggested by ISO/ASTM standards [37], using the perspective from the viewing window looking down on the build plate for both machines. That is to say, the "front" and "back" of the build plate are the edges closest and farthest from the build chamber door, respectively. The M290 employs a 400 W Yb-fiber laser with a 1100 nm wavelength. The system is capable of rapidly rastering the laser across the build plate at speeds up to 7000 mm/s utilizing an F-θ lens, although typical fabrication speeds are a fraction of this. The M290 infill build parameters followed a bi-directional parallel scanning strategy and are outlined in Table 1. Ultra-high purity (UHP) argon gas ($[O_2]$<1000 ppm) is pumped through grated inlets with circular holes at the back of the build plate. This shielding gas system flows from back to front of the build plate where it is evacuated from the build chamber through an outlet and recirculated through the system. As seen in Fig. 1a, forty cuboid specimens were fabricated with the M290 system using LPW grade 23 Ti-6Al-4V powder stock. The LPW particle size distribution and chemical composition are shown in Table 2. Re-used powder was utilized during fabrication as fine particle agglomerates, which are more common in virgin powders, have been shown to increase defect populations and reduce the mechanical performance of LPBF components [38,39]. Specimen locations were distributed across the 625 mm^2 build plate surface in accordance with NASA recommendation [40]. Each specimen had a square cross-section, rotated 45° about the build axis, with an edge length of 14 mm and a height of 105 mm oriented vertically from the build surface. The prescribed build parameters were held constant for all specimens as the EOS M290 system default settings for Ti-6Al-4V fabrication. This ensured that comparative analysis between specimens would be independent of power schedule, geometry, and build orientation.

The DMP320 has a larger build envelope of 275×275×430mm (WxDxH) utilizing a bi-directional silicon strip powder deposition system. The DMP320 uses a 500 W Yb-fiber laser with a 1070 nm wavelength. The infill build parameters followed a bi-directional parallel scanning strategy and are outlined in Table 1. Before fabrication, the

DMP320 build chamber is evacuated. Then UHP argon gas is introduced, flowing over the build plate from front to back (reversed direction of the M290). An open outlet at the back of the build plate draws gas flow from a linear inlet jet parallel to the build surface at the front of the build chamber. The DMP320 system advertises argon gas flow with extremely low oxygen content ($[O_2] < 25$ ppm). Ninety-three specimens were fabricated on the DMP320 with re-used Tekmat ASTM grade 23 Ti-6Al-4V powder stock (Table 2). The build layout involved a combination of vertically built cylindrical and horizontally stacked cuboidal specimens as seen in Fig. 1b. The cylinders and cuboids had a cross-section diameter or square edge length of 13 mm, with a length of 94 mm along their long axis. Specimens were distributed across the build plate as five colonies of nine cylinders located at the four corners and the center of a rotated square build layout, connected by eight walls each containing six cuboidal specimens as seen in Fig. 1b. Similar to the M290 build, the DMP320 system default parameters for Ti-6Al-4V were used for all specimens.

After fabrication, both sets of specimens underwent a low temperature stress relief treatment in accordance with the best-practice recommendation of the manufacturers. The M290 specimens were heated to 704° C for one hour in an argon environment then air-cooled. The DMP320 specimens were heated for two hours at 663 ° C then slowly cooled in an inert environment. Both of these thermal treatments are expected to reduce residual stresses in LPBF Ti-6Al-4V to negligible levels [41].

2.2. Defect distribution quantification

To examine the build defects produced by the M290 and DMP320, X-ray CT was performed on a Zeiss Versa 520 micro-CT. A cylinder with height and diameter of 7 mm was scanned at the midpoint of each specimen's long axis as seen in Fig. 2. The center 12 mm of each specimen was reduced to a diameter of 9 mm via a turret lathe. This was done to improve the X-ray CT analysis, reducing cost and noise. The diameter of the reduced section was much larger than the diameter of the scanned volume ensuring that surface machining did not affect scan results. X-ray CT was performed on the reduced section with the following parameters: power of 10 W, current of 71.6μA, and an acceleration voltage of 140 kV. Approximately 1015 projections were collected on a scintillator detector rotating 360° around the specimen axis with 2.5–5 s exposure times for each scan. Voxel sizes were maintained at about 7μm, entailing approximately 785 M voxels per scan. 3D analysis of the CT data was performed via the software package ImageJ [42], where low density regions containing eight or more contiguous 7μm voxels were classified as build defects (an effective spherical diameter of 17μm). For reference, defects below a critical size of ∼ 26μm are thought to be inert with respect to their contribution to high cycle fatigue failures in LPBF T-6Al-4V [43]. Conversely, due to the relatively small defects found in LPBF Ti-6Al-4V, fatigue response is not governed by the largest or most geometrically detrimental defect as in traditional fracture mechanics [18,43,44]. For these reasons, the shape of the defects in each specimen are not considered in this work.

All forty specimens of the M290 build underwent CT scanning. As will be discussed in Section 3.1, the results of this scanning showed the most extreme deviation in defect populations were found near the edges of the build plate due to systemic asymmetries associated with the LPBF process. For this reason, and coupled with the cost of CT analysis, only nineteen of the ninety-three specimens (ten cuboids and nine cylinders) were examined from the edges of the DMP320 build plate. The defect populations were quantified using three metrics. The first was defect number density, or the number of defects meeting the criteria defined above per unit of scanned volume. The next was defect volume fraction, calculated by taking the ratio of the total defect volume to total scanned volume. The final metric was the effective diameter of individual defects. For each cluster of contiguous low density voxels within the scanned section meeting the build defect criteria defined above, an
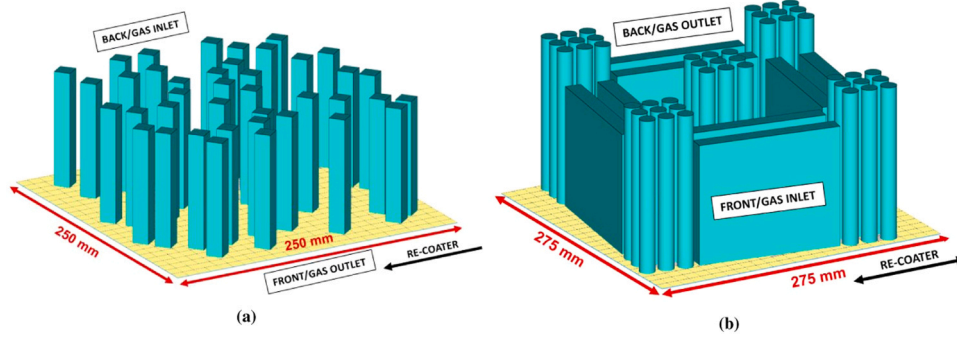
Table 1
Ti-6Al-4V infill build parameters for the M290 and DMP320 LPBF systems.

	Laser Power (W)	Scan Speed (mm/s)	Hatch Distance (μm)	Layer Thickness (μm)	Beam Diameter (μm)	Energy Density (J/mm^3)
M290	280	1200	140	30	100	55.6
DMP320	245	1250	82	60	85	39.8

Fig. 1. Build layouts for the Ti-6Al-4V specimens fabricated on (a) an EOS M290 and (b) a 3D Systems ProX DMP320 LPBF system.

Table 2
Particle size distribution (PSD) and chemical composition (wt%) of Ti-6Al-4V powders.

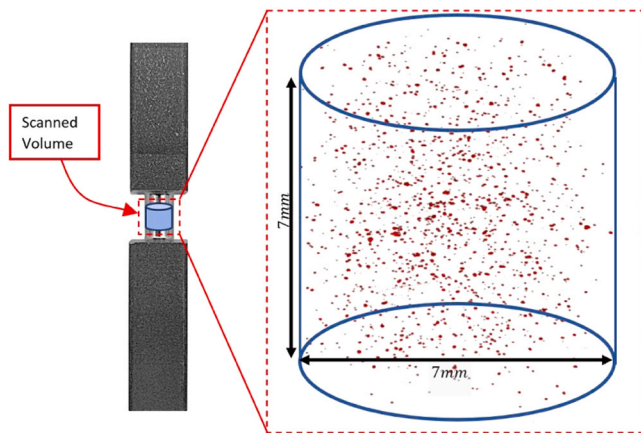|	PSD (μm)	Ti	Al	V	Fe	O	N	C	H
LPW	15–45	Bal.	6.4	4.0	0.2	0.12	0.02	0.02	0.002
Tekmat	20–53	Bal.	6.17	3.88	0.16	0.075	0.02	0.007	0.002

Fig. 2. Defect population in EOS M290 specimen 4 with reduced midsection for efficient CT imaging. The scanned cylinder has a diameter and height of 7 mm.

effective defect diameter was calculated by assuming the shape of these low density voxels' volume to be spherical. The effective defect diameter of each defect was then averaged for every specimen's scanned volume individually, and for all defects in every scanned specimens from the M290 and DMP320 builds as a whole.

3. Results and analysis

3.1. Defect populations

The goal of this work is to identify and compare the spatial dependency of fabrication quality produced by the LPBF systems studied here. Due to the differences in component geometry, build parameters, and powder composition detailed in section 2, no conclusion on the superiority of one system relative to the other can be established [5,17, 33]. For the two cases presented here (Table 3), the observed mean number density and volume fraction of defects in the components fabricated on the M290 were approximately an order of magnitude lower than those fabricated on the DMP320. Although more defects were observed in the DMP320 specimens, the average effective diameter of all defects measured in the M290 specimens was slightly larger (8.5%). Reiterating, the source of difference in average build quality between these two sets of specimens is not obvious to the authors as the

Table 3
Quantified defect populations in both LPBF systems.

Build		Defect Data	Specimen Data	
System	Measurement	Defect Diameter (μm)	Defect Volume Fraction (%)	Defect Number Density (mm^{-3})
DMP320	Average	4.12E+01	3.56E-02	7.26E+00
	Variance	1.70E-01	5.56E-04	1.70E+01
M290	Average	4.47E+01	3.74E-03	5.44E-01
	Variance	2.72E-01	4.01E-05	1.43E+00

discrepancies in build inputs creates too large of a parameter space for analysis. Contrastingly, this is not the case when considering the variability of defect populations among specimens fabricated from the same build with the above mentioned variables held constant. For this reason, the defect population dependence on build plate location within each build was analyzed separately. The resulting defect population trends and the degree of spatial dependency of the build quality identified within each build was then compared.

Considering the measured defect number density and volume fraction from the M290 build in Fig. 3a and c, it is clear that part quality is not spatially constant, but drastically reduced in a small region towards the back of the build plate. Specifically, the four specimens closest to the gas inlet (specimens 1–4) show an increased defect volume fraction by a factor ranging from 6 to 16 and an increased defect number density by a factor of 11–32 when compared to the average values from the remainder of the build (specimens 5–40). These same four specimens have an average effective defect diameter 14% smaller than the rest of the build. In other words, the specimens with highest number of defects have a reduced average defect diameter when compared to higher quality specimens. This observation might suggest that a separate mechanism could govern defect formation in this region of the build plate. Such a change in formation mechanism will be discussed further in Section 3.3.

Examining the CT results for the DMP320 in Figs. 3b and 3d, a clear region of poor fabrication quality is not initially obvious. At the back of the build plate near the shielding gas outlet, the two wall specimens (specimens 2 and 3) exhibit the highest defect number density and volume fraction throughout the build. This is consistent with the M290 data, indicating a region of reduced fabrication quality near the back of the build plate, i.e. close to the gas inlet in the M290 and outlet in the DMP320. The cylindrical specimen closest to the gas outlet (specimen 1)
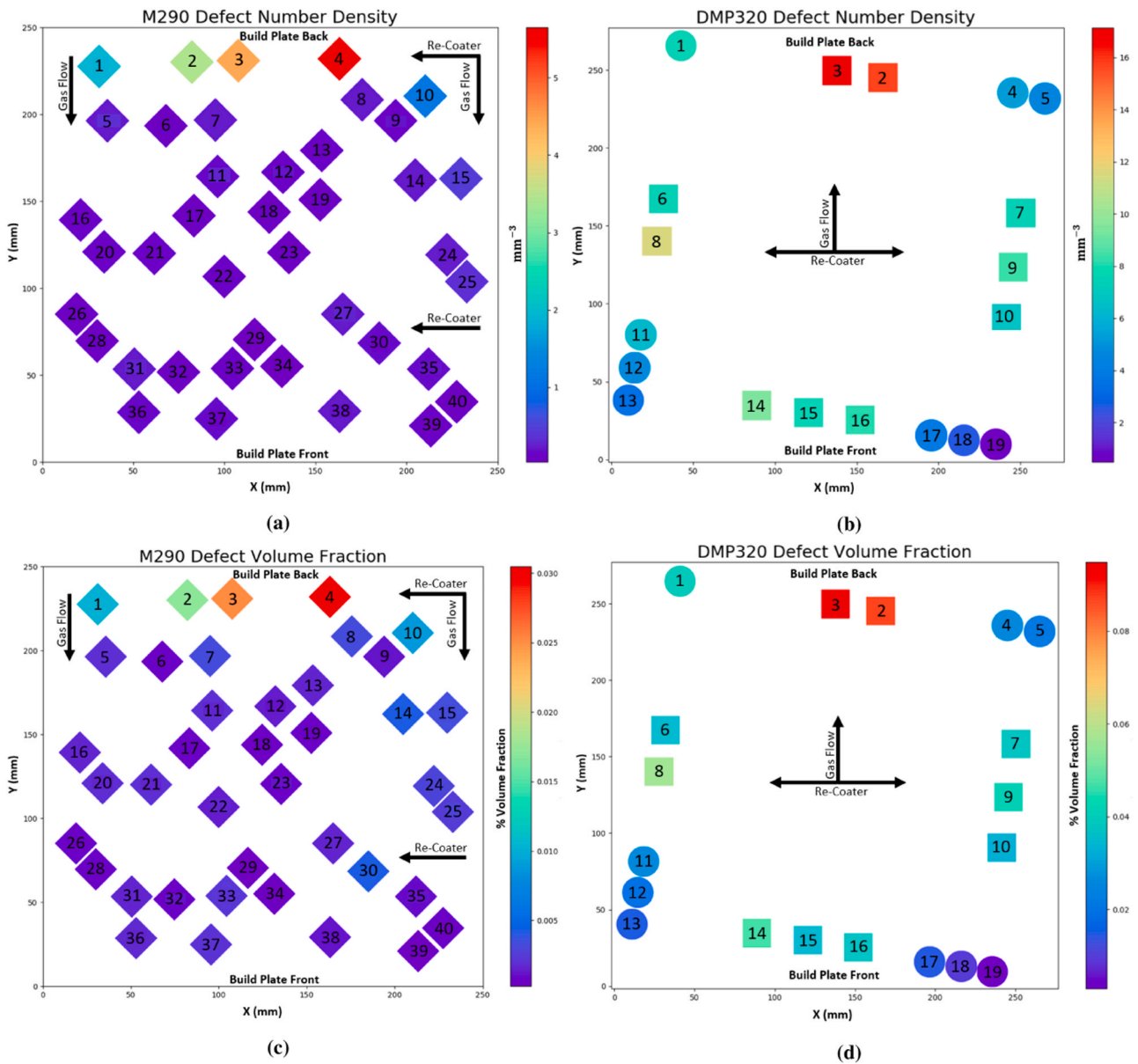
Fig. 3. Measured specimen defect number density across the build plate of the (a) EOS M290 and (b) 3D Systems ProX DMP320 build. Measured defect volume fraction across the build plate of the (c) EOS M290 and (d) 3D Systems ProX DMP320 build.
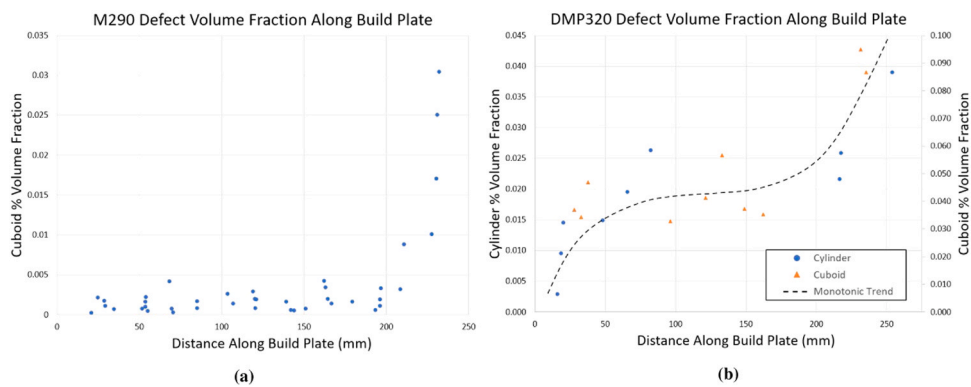

Fig. 4. Defect volume fraction in (a) M290 and (b) DMP320 specimens plotted as a function of distance along the build plate with 0 mm being the front of the build plate and 250 mm/275 mm being the back of the build plate for the M290 and DMP320 respectively. Note: The DMP320 specimens were plotted on separate axes to account for the effects of component geometry and build orientation on defect volume fraction.

deviates from this trend, exhibiting only average defect number density and volume fraction when compared to the overall build. This may be due to differences in geometry and build orientation between the cylindrical and cuboidal specimens in the DMP320 build [32]. Because the effects of build orientation and geometry are beyond the scope of this work, which is to investigate spatial variability while holding these variables constant, it is necessary to separate the two specimen types when analyzing build quality. Fig. 4b shows that upon separation by component type between two axes, a common trend for both geometries is observed. Unlike the M290 data which shows a small region containing a sudden and large deviations in part quality when compared to the rest of the build (Fig. 4a), the defect volume fraction in the DMP320 slowly increases with increased distance from the gas inlet. Despite the limited data presented in Fig. 4b, a strong positive correlation between defect volume fraction and distance along the build plate is quantified by a high Spearman's rank-order correlation coefficient ($\rho = 0.76$), shown to be statistically significant ($p = 0.00015$). With increased CT scanning this correlation would be expected to increase, although the absence of scanned specimens from the center of the build plate could deviate from the trend presented in Fig. 4b.

In addition to the sudden decrease in quality at the back of the build plate in the M290 versus a continuous trend of decreasing quality along the build plate in the DMP320, it is worthwhile to compare the degree to which location on the build plate causes deviation from the average build quality in both builds. In the DMP320, cylindrical specimens 1 and cuboidal specimens 2 and 3 show the lowest part quality when group geometries are analyzed separately. These specimens equate to an increased defect number density and volume fraction by a factor of approximately two. This, in contrast to the M290 build, is a much smaller deviation from the mean part quality, implying a reduced spatial dependence on fabrication quality in the DMP320.

Despite relative deviations from the mean part quality being far more extreme and localized in the M290, the total range of measured defect volume fractions within the DMP320 build is greater than the M290 due to the DMP320′s decreased average build quality. Treating each scanned specimen's measured percent defect volume fraction as a discrete data point, the range of defect volume fraction within each build due to spatial dependencies can be quantified by taking the difference between the maximum and minimum values. This range of measured defect volume fractions is 0.03% for the M290 and 0.092% for the DMP320. Comparing this metric, to previous studies examining part quality sensitivity to prescribed build parameters can be useful. Shange et al. examined the defect volume fraction in LPBF Ti-6Al-4V parallelepiped components as a function of local geometry by varying the overhang angle from the build plate [45]. Shange found that porosity was inversely proportional to the degree of overhang, with angles from 20° to 90° producing a percent volume fraction decrease of 0.05%. Elambasseril et al. investigated the defect volume fraction sensitivity to component build height in tall thin cylindrical Ti-6Al-4V specimens [30]. Using X-ray CT analysis Elambasseril showed changes in defect size, shape, and density towards the top of the cylinders due to heat build up in the components during fabrication. This change in percent defect volume fraction from the bottom third to the top third of the cylinders was 0.075%. Kasperovich et al. studied the effects of power schedule on defect volume fraction in LPBF components utilizing synchrotron tomography [10]. Specifically, the defect volume fraction measured in Ti-6Al-4V cubes as a function of hatch spacing, scan speed, and laser power were analyzed to bound optimal build parameters. The hatch distance, varied from 20 to 180μm, showed the smallest difference between the maximum and minimum defect volume fraction measured of 0.11%. Varying the laser power from 100 W to 200 W showed a increased volume fraction range of 0.81%. Lastly, the laser scan speed was increased from 200 mm/s to 1100 mm/s. This resulted in the largest volume fraction range of the three experiments of 2.29%. Contrasting the degree of spatial variability in defect populations measured here, which are independent of the prescribed build parameters, to the effects

of these parameters in the three studies cited above suggests that spatial dependency plays a considerable role on LPBF fabrication quality. This degree of variability is shown in Fig. 5, where it is clear that build plate location is as influential on defect formation as variables like overhang angle, hatch distance, and build height, but less important than laser power and velocity.[1] For this reason, future efforts to optimize component fabrication quality should also consider the spatial dependency of defect populations for a given LPBF system in addition to the prescribed build parameters.

3.2. Predicted fatigue response

In an attempt to provide context for the level of observed build plate variability, Li et al.'s [19] weakest link fatigue life model is considered. This model was experimentally validated by preforming fatigue testing of Ti-6Al-4V specimens in the "as-built" surface condition after undergoing a low temperature stress relief treatment, similar to the work presented here. Li found that increased internal defect populations in specimens with "as-built" surfaces from the same build were responsible for a reduction in fatigue life, although other working hypotheses for this decreased performance exist [46]. In this model "internal" refers to defects far from the boundary, in the bulk of the component, where defect quantification via CT analysis can be more accurately performed.

This weakest link model assumes a random fatigue life associated with each crack initiation site (i.e. defect), and a specimen life that is the minimum of its defects' fatigue lives. A relationship between the survival probability of a specimen and its number of crack initiating defects can then be written as

$$P(\log_{10} N_f > \log_{10} n_f) = S_\alpha(\log_{10} n_f) = (S_\beta(\log_{10} n_f))^\eta, \qquad (1)$$

where P is the survival function of a specimen, α, with a fixed number of crack initiating defects. S_β represents the survival function of a specimen, β, identical to α but with a homogeneously different defect population. η represents the ratio of the number of internal defects between the two specimens, i.e. the number of internal defects in specimen α divided by the number in specimen β. Although defects at or very close to the surface (where CT analysis becomes difficult) are expected to be greater in number than internal defects in the bulk, this model assumes that the ratio of internal defect densities is equal to the ratio of surface
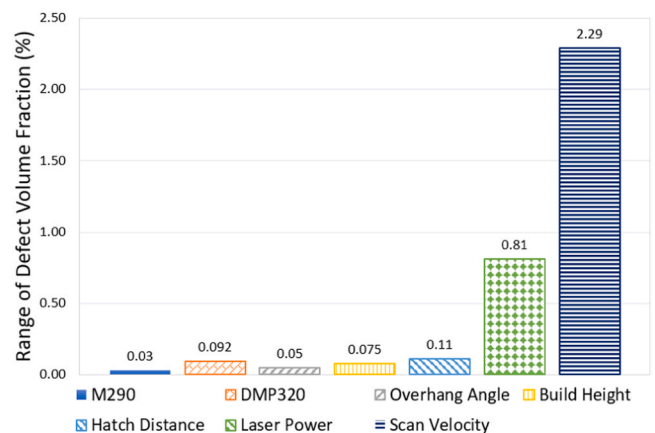

Fig. 5. Comparing the degree of variability using the range of defect volume fractions due to spatial dependency measured in this work with the results of five parametric studies of LPBF [10,30,45].

---

[1] Noting that this is true within the parametric boundaries of these studies, and that the relative importance of these variables may increase or decrease with large deviations from optimal parameters (e.g. very large hatch distance)

defect densities between two specimens. That is to say that $\eta_{bulk} = \eta_{surf}$. N_f is a random variable representing the number of cycles to failure of a particular specimen.

Assuming the presence of a large number of crack initiating defects, whose fatigue lives have independent and identically distributed (i.i.d.) attributes, asymptotic order statistics [47] provides a compact and useful description of the survival function for the specimens considered in this work, i.e. the three parameter Weibull distribution [48],

$$S(\log_{10} n_f) = e^{-\left(\frac{\log_{10} n_f - \theta}{\lambda}\right)^{\kappa}}, \tag{2}$$

where λ is associated with the variance of $\log_{10} N_f$, κ is the shape parameter describing failure rate with respect to $\log_{10} n_f$, and θ is the location parameter controlling the minimum observable value of $\log_{10} N_f$. Keeping with traditional fatigue literature, the stress amplitude (σ_a) is assumed to be linearly related to number of cycles to failure (N_f) in $\log_{10} - \log_{10}$ space, with the variance of these logarithms assumed to be independent of one another during high cycle fatigue [49,50]. Therefore, the stress dependency of fatigue life must be independent of κ and λ, being described only by the location parameter, θ, in the following form,

$$\theta = A\log_{10}\sigma_a + B - \lambda\Gamma\left(1 + \frac{1}{\kappa}\right), \tag{3}$$

where κ is governed by the total data variability, and A and B are governed by the stress dependence and the mean of the fatigue data, respectively.

The parameters for equation 2 and 3 were validated for stress relieved LPBF Ti-6Al-4V in the "as-built" surface condition and are available in [19]. Assuming an "as-built" surface condition, the predicted number of cycles at which 95% of specimens considered here are expected to survive as a function of stress amplitude and defect number densities can be calculated by plugging equations 2 and 3 into equation 1. Comparing the specimens containing high defect number density (specimens 1–4 for the M290 and specimens 1–3 for the DMP320) relative to the average defect number density of the remaining specimens in each build is plotted in Fig. 6. The high quality (i.e. low defect number density) parts away from the back of the build plate on the M290 (specimens 5–40) are predicted to perform the best. Following these specimens were the four lower quality M290 specimens (specimens 1–4) with the second lowest defect number density. Having an increased defect number density, the DMP320 specimens were predicted
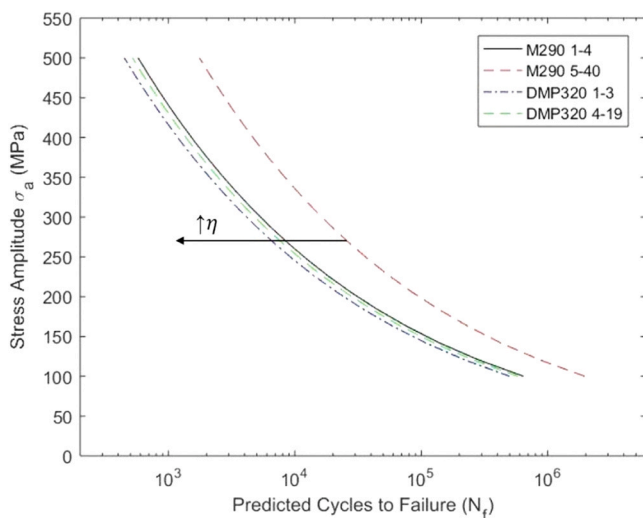

Fig. 6. Weakest link fatigue life predictions using measured defect number density data from X-ray CT scans.

to perform the worst. Although a large reduction in fatigue life is expected for the DMP320 specimens, the difference between specimens 1–3 and 4–19 is small when compared to the two sets from the M290. This again is a result of the low build plate variability of the DMP320 specimens when compared to the high build plate variability in the M290 build.

3.3. Role of shielding gas

Due to the aforementioned dependence of component quality on build plate location observed in both commercial machines, asymmetrical aspects of the LPBF systems are examined here in an attempt to elucidate causation. One inherent asymmetry in both machines is the laser incidence angle. The laser housing is centered above the build plate creating a decreased laser incidence angle as the scan progresses radially outward towards the boundary of the build plate. This change in incidence angle could theoretically impact defect formation towards the edges of the build plate. However, no such trend in defect populations was observed. Another source of imbalance during LPBF is the deposition of powder layers. The effects re-coater direction and powder flowability on part quality have been reported during LPBF [38]. In both the M290 and DMP320, powder is deposited by the re-coater in a lateral direction, orthogonal to principle gas flow direction. Once again the CT data presented here does not suggest such a lateral trend in defect populations which indicates layer deposition is not responsible for spatial dependencies on fabrication quality. The final asymmetry considered was the shielding gas velocity field which moves back to front in the M290, and front to back in the DMP320. The CT results do show specimen defect distribution variations along the gas flow axis, with high deviations from mean build quality near the inlet of the M290 build and to a lesser extent near the outlet in the DMP320. For this reason, the shielding gas velocity field for both machines is considered here.

Shielding gas is standard during LPBF fabrication to avoid oxidation and remove by-products originating from the melt pool, e.g. molten ejections and powder particles entrained in the vapor plume [51–54]. If by-products are not sufficiently removed from the laser's path, scattering can decrease the energy input to the melt pool resulting in lack of fusion defects [51,55,56]. Furthermore, powder particles and spatter ejection from the melt pool, not sufficiently removed from the build chamber via shielding gas entrainment, can be redeposited on the build plate. Large redeposited particles can increase surface roughness and interfere with energy input and powder distribution, creating lack of fusion defects [51,52,57]. Shielding gas analysis exists in the literature for a variety of LPBF machines with the quality of these velocity fields correlating to melt pool geometry, component density, and defect populations [55,56,58]. A homogeneous gas stream with velocities capable of removing by-products from the build chamber, without deposited powder disturbance, is optimal during LPBF fabrication.

To examine the velocity fields in both systems, computational fluid dynamics (CFD) modeling was performed. Due to the absence of a defect population dependency on lateral movement across the build plate in either system, a cross-section of the entire build chamber intersecting the center of the build plate, parallel with the gas flow direction was considered. Steady-state single-phase CFD analysis was performed for both build chamber geometries to model the shielding gas systems' effectiveness relative to recorded CT build plate defect population spatial variability. The Reynolds Averaged Navier-Stokes (RANS) equations and the standard shear transport (SST) κ-ω turbulence model [53,59,60] was implemented in ANSYS Fluent [61]. The argon gas flow was assumed to be incompressible, with a low Mach number ~ 0.02 [57, 62,63]. All walls of the build chamber were modeled with no-slip conditions prescribed [62,63]. Rectangular and triangular linear elements were used to mesh the build chamber, augmented by fifteen inflation layers at the domain boundary. An iterative solver was implemented to perform the simulation, with the scaled residuals of continuity, velocity,

energy, κ, and ω used as metrics of convergence.

During the M290 fabrication, the default settings for Ti-6Al-4V argon gas flow were used. The EOS engineering team provided the following details regarding the shielding gas system in the M290. This entailed a total volumetric shielding gas flow rate of 65.4 m³/hr. The M290 system divides the total flow among two inlets. The primary inlet is located at the bottom of the back wall of the build chamber, spanning the width of the build plate, with flow directed horizontally over the build surface. This inlet consumes approximately 60% of the total flow, creating a gas stream which functions to remove ejected particles and process by-products from the laser-powder interaction zone and out of the build chamber. The secondary inlet is a small circular nozzle centered at the top of the rear build chamber wall. This lens-clearing nozzle provides a continuous gas stream over the protective glass window housing the F-θ lens on the build chamber ceiling. Although maintaining a glass window free from debris is important to the functionality of the system, this stream is not expected to affect the gas stream near the laser-powder interaction zone and was not considered in this analysis. Modeling the primary flow rate of 39.2 m³/h, a velocity boundary condition of 4.6 m/s was applied at each circular 3.5 mm diameter hole of the grated primary inlet. With this geometry and velocity, a percent turbulent intensity and hydraulic diameter of 6% and 3.5 mm respectively were applied as initial conditions. The authors acknowledge an assumption of uniform velocity at all inlet holes may not be fully representative of the nozzle's true velocity. However, large deviations between individual nozzle hole velocities are not expected as the gas pathway before the inlet grate is long and does not have sharp cross-sectional dilations/curvature. This is assumed to produce a relatively homogeneous cross-sectional velocity profile before the shielding gas reaches the grated inlet cover.

Initial atmospheric pressure conditions were applied to the numerical domain. A cross-section of the build chamber velocity field magnitude from the prospective of the right side of the build chamber is shown in Fig. 7a. Towards the back of the build chamber, a large high-velocity laminar eddy is observed near the inlet. This circular flow deviates from the boundary layer flow parallel to the build plate surface. The jet stream continues across the build plate until boundary layer separation and evacuation out of the build chamber occurs through the outlet. This circular flow region near the inlet will entrain and locally circulate by-products formed by the melting of particles, causing scattering of the laser and thus lack of fusion defects. Additionally, small particles and

molten ejection circulated in the laminar eddy will be locally redeposited, causing inhomogeneities in powder layer thickness which will also contribute to lack of fusion defect formation. The shift in defect formation mechanisms from that of sub-optimal build parameters described in Section 1 to by-product laser scattering and/or redeposition onto the build plate could be responsible for the measured decrease in effective defect diameter in this region, discussed in Section 3.1. Comparing the back row of specimens in Figs. 3a, 3c, and 4a to the bottom right corner of Fig. 7a, a clear correlation between the region of circular flow (i.e. the laminar eddy in Fig. 7b) and measured increases in both defect volume fraction and number density are present. This fluctuation in gas velocity field is the source of the high deviations in specimen quality for specimens fabricated within the laminar eddy when compared to specimens fabricated elsewhere on the build plate experiencing boundary layer flow parallel to the build plate.

In contrast to the M290, the DMP320 gas flow driving force is a negative pressure maintained at the outlet. The DMP320 Ti-6Al-4V argon gas flow settings were built into the machine software and are not available to the authors, as this information is considered proprietary by 3D Systems. Accordingly, a parametric study was necessary to examine the effects of the pressure boundary condition prescribed at the outlet on velocity field shape and magnitude. It was found that as the magnitude of the pressure boundary condition was increased so did the gas velocity, but the general shape and trends of the gas flow field remained constant over the examined range of −25 Pa to −500 Pa. The final pressure boundary condition of −70 Pa was applied to the outlet with a turbulent intensity and hydraulic diameter of 5% and 15 mm respectively. This pressure was chosen to produce mean stream velocities at the center of the build plate approximately equal to the M290 model. Unlike the M290, the resulting DMP320 velocity field (Fig. 7c) does not present a clear explanation for the decreasing specimen quality towards the back of the build plate. The velocity field shows boundary layer coverage of the full build plate, free of large eddies close to the laser-powder interaction zone. This homogeneous shielding gas field is believed to be responsible for the improved consistency in specimen quality across the build plate when compared to the M290 build.

One potential explanation for the increasing number of defects in specimens towards the back of the build chamber is that by-products could be more easily entrained in a recirculated flow above the build plate in the DMP320. This can occur when ejected particle velocities are high or the bulk flow stream is thin, allowing the particle to pass through
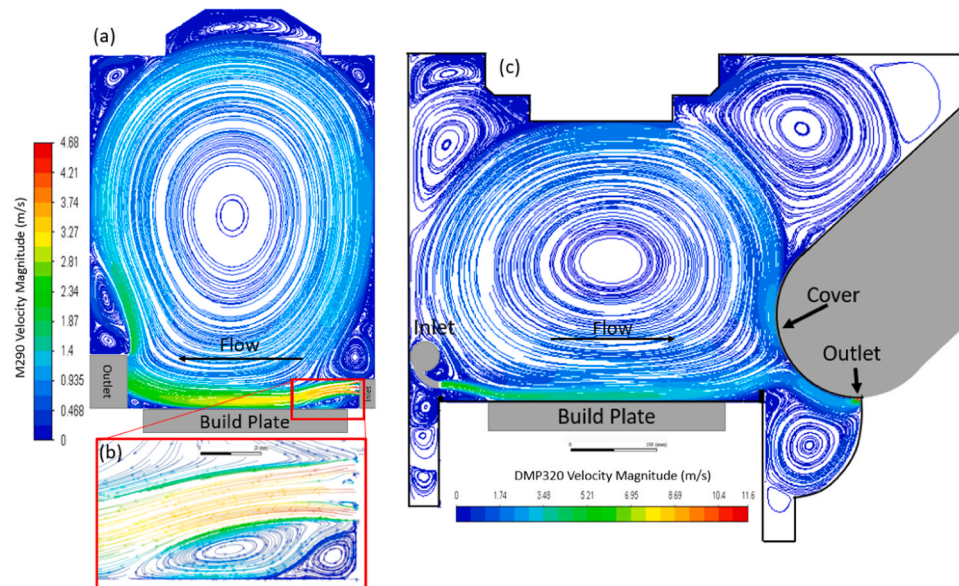

Fig. 7. Cross-section of build chamber gas velocity field looking from the right side (i.e. down the axis of the re-coater) of the build chamber for the (a) M290 with the gas eddy highlighted in red and (c) DMP320. A detailed view of the gas eddy in the M290 is shown in (b).

the primary stream and be circulated in the build chamber before eventual redeposition on the build plate [53]. Utilizing zero mass particle tracing, the thickness of each gas stream which flows directly to the outlet and is not first recirculated above the build plate was measured. The stream thickness for the M290 was 21 mm and 11.5 mm for the DMP320. This analysis suggests that recirculatory particle entrainment is more likely in the DMP320. Due to the direction of the gas flow in the DMP320, recirculated particles are expected to be deposited with increasing density towards the back of the build plate which is consistent with the observed gradual decrease in part quality moving away from the gas inlet. Another potential explanation for the gradual increases in defect number density and volume fraction towards the end of the shielding gas stream is a reduced velocity. Reduced shielding gas velocity has been observed in other LPBF systems to be inversely proportional to part density, as insufficient velocities will not have enough drag force to entrain and remove by-products from the build chamber [51,53,57]. As can be seen in both systems, the velocity fields decrease moving away from the gas inlet. These effects could be responsible for the small increase in the DMP320 defect population and would not be as obvious in the M290 due to the overshadowing effect of the eddy.

A possible solution for inconsistent component fabrication across the build plate is a redesign of the shielding gas systems to avoid the problems identified in this work. Such a redesign would ideally produce a homogeneous shielding gas velocity field covering the full surface of the build plate, absent of circular flow regions near the laser-powder interaction zone. This field would entail sufficient stream velocity and thickness to avoid recirculation of process by-products [51,53,57]. Specific improvements to these systems are beyond the scope of the work presented here, as potentially important variables are currently unknown to the authors (e.g. cost, manufacturability, and material selection). For this reason, only qualitative recommendations are made. In the EOS M290, geometrical improvements could be made near the primary inlet to eliminate the detrimental laminar gas eddies. Reducing spatial variability in part quality for the DMP320 are less clear. This could potentially be achieved by redesigning the gas inlet geometry, resulting in a thicker jet stream across the build plate. An increased jet stream thickness could reduce the amount of gas recirculated up into the build chamber before reaching the outlet, producing less bi-product redeposition along the gas flow axis.

4. Conclusion

A major factor limiting the broader qualification and implementation of LPBF components for fracture critical applications is the existence of defect populations formed during fabrication [6]. An extensive research effort has been conducted to link formation of these defects to geometry and material specific build parameters. Far less work has been done to understand defect population baseline variability across the build plate. In this work, Ti-6Al-4V specimens were fabricated on two common commercial LPBF systems, i.e EOS M290 and 3D Systems ProX DMP320. The defect populations were examined with the use of X-ray CT, with clear spatial dependency of part quality observed across the build plate in both machines. The M290 showed higher part quality deviations from the rest of build in four of the specimens located in a small region towards the gas inlet. Similarly the DMP320 exhibited a less extreme, but continuously decreasing, part quality moving towards the back of the build plate. For both builds, the deviation in part quality was shown to be comparable in magnitude to other commonly studied LPBF build parameters such as hatch spacing, build height, and component geometry, but less important than laser power and scanning speed. To show the potential effects of these variations on mechanical properties in stress relieved LPBF Ti-6Al-4V with as-built surface condition, a weakest link model was implemented to examine expected fatigue performance. The predicted fatigue life decreases due to increased regions of defect number density across the build plate were found to be substantial. Finally, possible causes of inhomogeneous defect

populations were investigated by examining the fundamental asymmetries of these LPBF systems. For the M290, a large eddy in the shielding gas velocity field was observed near the inlet, corresponding to the same region where poor part quality was measured. For the DMP320 a clear explanation for spatially varied part quality due to the shielding gas field was not as clear, as the field maintained boundary layer flow across the build plate. This homogeneous flow is assumed to be responsible for increased consistency observed in the DMP320 specimens when compared to the M290 build. The authors hypothesize that the reduced defect population variability observed in the DMP320 could be a result of recirculation entrainment and loss of shielding gas velocity field towards the outlet. For a truly homogeneous build quality independent of component location, shielding gas systems in both machines are recommended for redesign to produce a more consistent flow.

CRediT authorship contribution statement

T.P. Moran: Conceptualization, Methodology, Software, Investigation, Formal analysis, Writing – review & editing. **D.H. Warner:** Conceptualization, Methodology, Formal analysis, Resources, Writing. **A. Soltani-Tehrani:** Conceptualization, Writing – review & editing. **N. Shamsaei:** Conceptualization, Resources, Supervision, Writing – review & editing. **N. Phan:** Conceptualization, Resources, Supervision, Writing – review & editing.

Declaration of Competing Interest

The authors declare that they have no known competing financial interests or personal relationships that could have appeared to influence the work reported in this paper.

Acknowledgements

References

[1] D. Robinson, A. Lagnau, W. Boon, Innovation pathways in additive manufacturing: Methods for tracing emerging and branching paths from rapid prototyping to alternative applications, Technol. Forecast. Soc. Change 146 (2019) 733–750.

[2] W.E. Frazier, Metal additive manufacturing: a review, J. Mater. Eng. Perform. 23 (6) (2014) 1917–1928.

[3] B. Piascik, J. Vickers, D. Lowry, S. Scotti, J. Stewart, A. Calomino, Materials, structures, mechanical systems, and manufacturing roadmap, NASA TA (2012), 12-2.

[4] A.S. Keys, The role of advanced manufacturing in our journey to mars, NASA MSFC-E-DAA-TN39445 (2017).

[5] Y. Zhang, L. Wu, X. Guo, S. Kane, Y. Deng, Y. Jung, J. Lee, J. Zhang, Additive manufacturing of metallic materials: a review, J. Mater. Eng. Perform. 27 (1) (2018) 1–13.

[6] M. McElroy, R. Patin, S. Luna, Fracture control for additive manufactured spacecraft structures, Proc. 70th Int. Astronaut. Congr. (2019).

[7] T. Mukherjee, T. DebRoy, Mitigation of lack of fusion defects in powder bed fusion additive manufacturing, J. Manuf. Process. 36 (2018) 442–449.

[8] N. Sanaei, A. Fatemi, N. Phan, Defect characteristics and analysis of their variability in metal L-PBF additive manufacturing, Mater. Des. 182 (2019), 108091.

[9] M. Tang, P.C. Pistorius, J.L. Beuth, Prediction of lack-of-fusion porosity for powder bed fusion, Addit. Manuf. 14 (2017) 39–48.

[10] G. Kasperovich, J. Haubrich, J. Gussone, G. Requena, Correlation between porosity and processing parameters in TiAl6V4 produced by selective laser melting, Mater. Des. 105 (2016) 160–170.

[11] S. Tammas-Williams, H. Zhao, F. Léonard, F. Derguti, I. Todd, P.B. Prangnell, XCT analysis of the influence of melt strategies on defect population in Ti-6Al-4V components manufactured by selective electron beam melting, Mater. Charact. 102 (2015) 47–61.

[12] A.A. Martin, N.P. Calta, S.A. Khairallah, J. Wang, P.J. Depond, A.Y. Fong, V. Thampy, G.M. Guss, A.M. Kiss, K.H. Stone, Dynamics of pore formation during

laser powder bed fusion additive manufacturing, Nat. Commun. 10 (1) (2019) 1–10.

[13] A.M. Kiss, A.Y. Fong, N.P. Calta, V. Thampy, A.A. Martin, P.J. Depond, J. Wang, M. J. Matthews, R.T. Ott, C.J. Tassone, Laser-induced keyhole defect dynamics during metal additive manufacturing, Adv. Eng. Mater. 21 (10) (2019), 1900455.

[14] C.L.A. Leung, S. Marussi, M. Towrie, J. delValGarcia, R.C. Atwood, A.J. Bodey, J. R. Jones, P.J. Withers, P.D. Lee, Laser-matter interactions in additive manufacturing of stainless steel SS316L and 13-93 bioactive glass revealed by in situ x-ray imaging, Addit. Manuf. 24 (2018) 647–657.

[15] W.H. Yu, S.L. Sing, C.K. Chua, C.N. Kuo, X.L. Tian, Particle-reinforced metal matrix nanocomposites fabricated by selective laser melting: a state of the art review, Prog. Mater. Sci. 104 (2019) 330–379.

[16] P. Li, D.H. Warner, N. Phan, Predicting the fatigue performance of an additively manufactured Ti-6Al-4V component from witness coupon behavior, Addit. Manuf. 35 (2020), 101230.

[17] J.W. Pegues, S. Shao, N. Shamsaei, N. Sanaei, A. Fatemi, D.H. Warner, P. Li, N. Phan, Fatigue of additive manufactured Ti-6Al-4V, part I: the effects of powder feedstock, manufacturing, and post-process conditions on the resulting microstructure and defects, Int. J. Fatigue 132 (2020), 105358.

[18] P. Li, D.H. Warner, J.W. Pegues, M.D. Roach, N. Shamsaei, N. Phan, Investigation of the mechanisms by which hot isostatic pressing improves the fatigue performance of powder bed fused Ti-6Al-4V, Int. J. Fatigue 120 (2019) 342–352.

[19] P. Li, D.H. Warner, J.W. Pegues, M.D. Roach, N. Shamsaei, N. Phan, Towards predicting differences in fatigue performance of laser powder bed fused Ti-6Al-4V coupons from the same build, Int. J. Fatigue 126 (2019) 284–296.

[20] P. Li, D.H. Warner, A. Fatemi, N. Phan, Critical assessment of the fatigue performance of additively manufactured Ti-6Al-4V and perspective for future research, Int. J. Fatigue 85 (2016) 130–143.

[21] G. Qian, Z. Jian, X. Pan, F. Berto, In-situ investigation on fatigue behaviors of Ti-6Al-4V manufactured by selective laser melting, Int. J. Fatigue 133 (2020), 105424.

[22] U.S. Bertoli, A.J. Wolfer, M.J. Matthews, J.R. Delplanque, J.M. Schoenung, On the limitations of volumetric energy density as a design parameter for selective laser melting, Mater. Des. 113 (2017) 331–340.

[23] H. Gong, K. Rafi, H. Gu, T. Starr, B. Stucker, Analysis of defect generation in Ti-6Al-4V parts made using powder bed fusion additive manufacturing processes, Addit. Manuf. 1 (2014) 87–98.

[24] L. Scime, J. Beuth, Melt pool geometry and morphology variability for the inconel 718 alloy in a laser powder bed fusion additive manufacturing process, Addit. Manuf. 29 (2019), 100830.

[25] J. Ciurana, L. Hernandez, J. Delgado, Energy density analysis on single tracks formed by selective laser melting with CoCrMo powder material, Int. J. Adv. Manuf. Technol. 68 (5–8) (2013) 1103–1110.

[26] W. Di, Y. Yongqiang, S. Xubin, C. Yonghua, Study on energy input and its influences on single-track, multi-track, and multi-layer in SLM, Int. J. Adv. Manuf. Technol. 58 (9–12) (2012) 1189–1199.

[27] D.S. Ertay, H. Ma, and M. Vlasea.Correlative beam path and pore defect space analysis for modulated powder bed laser fusion process. In Proceedings of the 29th Annual International Solid Freeform Fabrication Symposium, 274–284.

[28] Q. Han, H. Gu, S. Soe, R. Setchi, F. Lacan, J. Hill, Manufacturability of AlSi10Mg overhang structures fabricated by laser powder bed fusion, Mater. Des. 160 (2018) 1080–1095.

[29] B. Lane, E. Whitenton, S. Moylan, Multiple sensor detection of process phenomena in laser powder bed fusion, Thermosense (2016).

[30] J. Elambasseril, S.L. Lu, Y.P. Ning, N. Liu, J. Wang, M. Brandt, H.P. Tang, M. Qian, 3D characterization of defects in deep-powder-bed manufactured Ti-6Al-4V and their influence on tensile properties, Mater. Sci. Eng. 761 (2019), 138031.

[31] A.R. Nassar, J.S. Keist, E.W. Reutzel, T.J. Spurgeon, Intra-layer closed-loop control of build plan during directed energy additive manufacturing of Ti-6Al-4V, Addit. Manuf. 6 (2015) 39–52.

[32] R. Shrestha, N. Shamsaei, M. Seifi, N. Phan, An investigation into specimen property to part performance relationships for laser beam powder bed fusion additive manufacturing, Addit. Manuf. 29 (2019), 100807.

[33] T.P. Moran, D.H. Warner, N. Phan, Scan-by-scan part-scale thermal modelling for defect prediction in metal additive manufacturing, Addit. Manuf. (2020) 101667.

[34] S.A. Khairallah, A.T. Anderson, A. Rubenchik, W.E. King, Laser powder-bed fusion additive manufacturing: physics of complex melt flow and formation mechanisms of pores, spatter, and denudation zones, Acta Mater. 108 (2016) 36–45.

[35] J.M. Solberg, N.E. Hodge, R.M. Ferencz, I.D. Parsons, M.A. Puso, M.A. Havstad, R. A. Whitesides, and A.P. Wemhoff.Diablo user manual livermore, CA. Technical report, Report No. LLNL-SM-651163, 2014.

[36] T.P. Moran, P. Li, D.H. Warner, N. Phan, Utility of superposition-based finite element approach for part-scale thermal simulation in additive manufacturing, Addit. Manuf. 21 (2018) 215–219.

[37] ASTM International,, 2012.

[38] A. Soltani-Tehrani, J. Pegues, N. Shamsaei, Fatigue behavior of additively manufactured 17-4 PH stainless steel: the effects of part location and powder re-use, Addit. Manuf., page 101398 (2020).

[39] P.E. Carrion, A. Soltani-Tehrani, N. Phan, N. Shamsaei, Powder recycling effects on the tensile and fatigue behavior of additively manufactured Ti-6Al-4V parts, JOM 71 (3) (2019) 963–973.

[40] Specification for Control and Quantification of Laser Powder Bed Fusion Metallurgical Processes. Standard, National Aeronautics and Space Administration, Marshall Space Flight Center, Alabama, USA, October 2017.

[41] G.M. TerHaar, T.H. Becker, Low temperature stress relief and martensitic decomposition in selective laser melting produced Ti6Al4V, Mater. Des. Process. Commun. (2020) e138.

[42] J. Schindelin, I. Arganda-Carreras, E. Frise, V. Kaynig, M. Longair, T. Pietzsch, S. Preibisch, C. Rueden, S. Saalfeld, B. Schmid, Fiji: an open-source platform for biological-image analysis, Nat. Methods 9 (7) (2012) 676–682.

[43] S. Leuders, M. Vollmer, F. Brenne, T. Tröster, T. Niendorf, Fatigue strength prediction for titanium alloy TiAl6V4 manufactured by selective laser melting, Metall. Mater. Trans. A 46 (9) (2015) 3816–3823.

[44] S. Tammas-Williams, P.J. Withers, I. Todd, P.B. Prangnell, The influence of porosity on fatigue crack initiation in additively manufactured titanium components, Sci. Rep. 7 (1) (2017) 1–13.

[45] M. Shange, I. Yadroitsava, S.P.I. Yadroitsev, A. duPlessis, Determining the effect of surface roughness and porosity at different inclinations of LPBF parts, RAPDASA 2019 Proc., Pages 40-51 (2019).

[46] J. Pegues, M. Roach, R.S. Williamson, N. Shamsaei, Surface roughness effects on the fatigue strength of additively manufactured Ti-6Al-4V, Int. J. Fatigue 116 (2018) 543–552.

[47] J. Galambos.The asymptotic theory of extreme order statistics. Technical report, 1978.

[48] W. Weibull, Wide applicability, J. Appl. Mech. 103 (730) (1951) 293–297.

[49] O.H. Basquin, The exponential law of endurance tests, Proc. Am. Soc. Test. Mater. 10 (1910) 625–630.

[50] R.I. Stephens, A. Fatemi, R.R. Stephens, H.O. Fuchs. Metal Fatigue in Engineering, John Wiley & Sons,, 2000.

[51] A. Ladewig, G. Schlick, M. Fisser, V. Schulze, U. Glatzel, Influence of the shielding gas flow on the removal of process by-products in the selective laser melting process, Addit. Manuf. 10 (2016) 1–9.

[52] S. Ly, A.M. Rubenchik, S.A. Khairallah, G. Guss, M.J. Matthews, Metal vapor micro-jet controls material redistribution in laser powder bed fusion additive manufacturing, Sci. Rep. 7 (1) (2017) 1–12.

[53] A.M. Philo, C.J. Sutcliffe, S. Sillars, J. Sienz, S.G.R. Brown, N.P. Lavery, A study into the effects of gas flow inlet design of the renishaw AM250 laser powder bed fusion machine using computational modelling, Solid Free. Fabr. Symp. (2017).

[54] A.T. Sutton, C.S. Kriewall, M.C. Leu, J.W. Newkirk, B. Brown, Characterization of laser spatter and condensate generated during the selective laser melting of 304L stainless steel powder, Addit. Manuf. 31 (2020), 100904.

[55] C.J. Kong, C.J. Tuck, I.A. Ashcroft, R.D. Wildman, R. Hague, High density Ti6Al4V via SLM processing: microstructure and mechanical properties, Int. Solid Free. Fabr. Symp., Vol. 36 (2011) 475–483.

[56] B. Ferrar, L. Mullen, E. Jones, R. Stamp, C.J. Sutcliffe, Gas flow effects on selective laser melting (SLM) manufacturing performance, J. Mater. Process. Technol. 212 (2) (2012) 355–364.

[57] A.M. Philo, D. Butcher, S. Sillars, C.J. Sutcliffe, J. Sienz, S.G.R. Brown, N.P. Lavery, A multiphase CFD model for the prediction of particulate accumulation in a laser powder bed fusion process. TMS Annual Meeting & Exhibition, Springer,, 2018, pp. 65–76.

[58] J. Reijonen, A. Revuelta, T. Riipinen, K. Ruusuvuori, P. Puukko, On the effect of shielding gas flow on porosity and melt pool geometry in laser powder bed fusion additive manufacturing, Addit. Manuf. 32 (2020), 101030.

[59] F. Menter, Two-equation eddy-viscosity turbulence models for engineering applications, AIAA J. 32 (8) (1994) 1598–1605.

[60] P. Bidare, I. Bitharas, R.M. Ward, M.M. Attallah, A.J. Moore, Fluid and particle dynamics in laser powder bed fusion, Acta Mater. 142 (2018) 107–120.

[61] ANSYS Fluent. Ansys fluent. Academic Research. Release, 14, 2015.

[62] P. Wen, Y. Qin, Y. Chen, M. Voshage, L. Jauer, R. Poprawe, J.H. Schleifenbaum, Laser additive manufacturing of Zn porous scaffolds: Shielding gas flow, surface quality and densification, J. Mater. Sci. Technol. 35 (2) (2019) 368–376.

[63] Y. Chen, G. Vastola, Y.W. Zhang, Optimization of inert gas flow inside laser powder bed fusion chamber with computational fluid dynamics. 29th Annu. Int. Solid Free. Fabr. Symp. - Addit. Manuf. Conf., Austin, TX, USA, 2018, pp. 1931–1939.